PAPER • OPEN ACCESS

MCTDH-X: The multiconfigurational time-dependent Hartree method for indistinguishable particles software

View the article online for updates and enhancements.

IOP ebooks™

Bringing together innovative digital publishing with leading authors from the global scientific community.

Start exploring the collection−download the first chapter of every title for free.

Quantum Science and Technology

PAPER

OPEN ACCESS

MCTDH-X: The multiconfigurational time-dependent Hartree method for indistinguishable particles software

Rui Lin[1] , Paolo Molignini[1], Luca Papariello[2], Marios C Tsatsos[3], Camille Lévêque[4,5], Storm E Weiner[6], Elke Fasshauer[7] , R Chitra[1] and Axel U J Lode[8]

1 Institute for Theoretical Physics, ETH Zurich, 8093 Zurich, Switzerland
2 Research Studio Data Science, RSA FG, A-1090 Vienna, Austria
3 São Carlos Institute of Physics, University of São Paulo, PO Box 369, 13560-970, São Carlos, SP, Brazil
4 Vienna Center for Quantum Science and Technology, Atominstitut, TU Wien, Stadionallee 2, A-1020 Vienna, Austria
5 Wolfgang Pauli Institute c/o Faculty of Mathematics, University of Vienna, Oskar-Morgenstern Platz 1, A-1090 Vienna, Austria
6 Department of Physics, UC Berkeley, Berkeley, CA, United States of America
7 Department of Physics and Astronomy, Ny Munkegade 120, building 1520, 630, DK-8000 Aarhus C, Denmark
8 Institute of Physics, Albert-Ludwig University of Freiburg, Hermann-Herder-Strasse 3, D-79104 Freiburg, Germany

E-mail: auj.lode@gmail.com

Abstract

We introduce and describe the multiconfigurational time-depenent Hartree for indistinguishable particles (MCTDH-X) software, which is hosted, documented, and distributed at http://ultracold.org. This powerful tool allows the investigation of ground state properties and dynamics of interacting quantum many-body systems in different spatial dimensions. The MCTDH-X software is a set of programs and scripts to compute, analyze, and visualize solutions for the time-dependent and time-independent many-body Schrödinger equation for indistinguishable quantum particles. As the MCTDH-X software represents a general solver for the Schrödinger equation, it is applicable to a wide range of problems in the fields of atomic, optical, molecular physics, and condensed matter systems. In particular, it can be used to study light–matter interactions, correlated dynamics of electrons in the solid state as well as some aspects related to quantum information and computing. The MCTDH-X software solves a set of nonlinear coupled working equations based on the application of the time-dependent variational principle to the Schrödinger equation. These equations are obtained by using an ansatz for the many-body wavefunction that is a expansion in a set of time-dependent, fully symmetrized bosonic ($X = B$) or fully anti-symmetrized fermionic ($X = F$) many-body basis states. It is the time-dependence of the basis set that enables MCTDH-X to deal with quantum dynamics at a superior accuracy as compared to, for instance, exact diagonalization approaches with a static basis, where the number of basis states necessary to capture the dynamics of the wavefunction typically grows rapidly with time. Herein, we give an introduction to the MCTDH-X software via an easy-to-follow tutorial with a focus on accessibility. The illustrated exemplary problems are hosted at http://ultracold.org/tutorial and consider the physics of a few interacting bosons or fermions in a double-well potential. We explore computationally the position-space and momentum-space density, the one-body reduced density matrix, Glauber correlation functions, phases, (dynamical) phase transitions, and the imaging of the quantum systems in single-shot images. Although a few particles in a double well potential represent a minimal model system, we are able to demonstrate a rich variety of phenomena with it. We use the double well to illustrate the fermionization of bosonic particles, the crystallization of fermionic particles, characteristics of the superfluid and Mott-insulator quantum phases in Hubbard models, and even dynamical phase transitions. We provide a complete set of input files and scripts to redo all computations in this paper at http://ultracold.org/data/tutorial_input_files.zip, accompanied by tutorial videos at https://tinyurl.com/tjx35sq. Our tutorial should guide the potential users to apply the MCTDH-X software also to more complex systems.

1. Introduction

The time-dependent many-body Schrödinger equation (TDSE) is a fundamental equation at the heart of many different fields of science: quantum chemistry, condensed matter, and atomic and molecular physics. Exact solutions to the TDSE exist only for model systems, like the time-dependent harmonic interaction model [1–4]. Even for the time-independent many-body Schrödinger equation (TISE), exact solutions are scarce [5–12]. These exact solutions, however, are in most cases not generalizable to current experiments or theoretical studies. To obtain solutions to the TISE and TDSE, numerical methods and their implementation in software are therefore indispensable. Due to the fundamental nature of the problem, many methods have been put forward —each with their advantages and shortcomings.

Examples of these numerical methods are the matrix-product-state and density-matrix-renormalization-group approaches, which employ a hierarchical partitioning of the many-body Hilbert space, and are particularly well-suited for one-dimensional lattice systems [13, 14]. Meanwhile, mean-field approaches like the time-dependent Hartree–Fock [15] and the time-dependent Gross–Pitaevskii methods [16–18] employ a drastically simplified approximation to the wavefunction of the state that ignores correlation effects.

Since the 1990s, when the multiconfigurational time-dependent Hartree approach [19–21] (MCTDH) was first put forward, the method has been applied very successfully in the field of theoretical chemistry, where systems involve coupled and distinguishable degrees of freedom. MCTDH enables the description of correlated wavefunctions; its ansatz for the wavefunction is a sum of all possible configurations of *distinguishable* degrees of freedom or particles in a set of time-dependent variationally-optimized single-particle functions. In 2003, the MCTDH method for indistinguishable fermions [22–24] (MCTDH-F) was formulated, and in 2007 the MCTDH method for indistinguishable bosons [25, 26] (MCTDH-B) followed. MCTDH-F and MCTDH-B can be formulated in a unified manner [27], where they share the same equations of motion; henceforth we will use the acronym MCTDH-X to refer to this unified algorithm, where X is either X = F or X = B.

Other notable members of the MCTDH-family of methods include the restricted active space-(RAS-) and multilayer- (ML-)methods: RAS-MCTDH-F [28], RAS-MCTDH-B [29, 30], ML-MCTDH [31–33], the ML-MCTDH method in (optimized) second quantized representation [34, 35], and the ML-MCTDH-X method [36]. Here, the 'ML-' prefix implies that a hierarchical format of the tensor representation of the many-body wavefunction is employed. For a review of multiconfigurational methods for the dynamics of indistinguishable particles including these multilayering and other methods, see [4].

In this article, we provide an introduction to the software implementation of MCTDH-X hosted and distributed at http://ultracold.org [3, 37, 38]. In particular, MCTDH-F can be applied to describe the correlated dynamics of electrons in atoms and molecules [39–43] or to describe ultracold atomic fermions [3,44,45,46]. MCTDH-B can be used to describe the many-body properties of ultracold atomic bosons with a focus on the phenomenon of fragmentation [47, 48], where the reduced density matrix of the many-boson state attains several significant eigenvalues [49–54] and, as a result, quantum fluctuations are non-negligible [55–59].

Below, we provide a tutorial-type introduction to the MCTDH-X software with a focus on simplicity and instructiveness. The MCTDH-X software, however, can achieve way more than in the examples we introduce below. The MCTDH-X software can deal with indistinguishable particles with internal degrees of freedom like spin [38], indistinguishable particles placed in a high-finesse optical cavity [57, 60–63], indistinguishable particles with long-range dipolar interactions [58, 59, 64, 65] and Hubbard (lattice) models [38]. Moreover, the MCTDH-X software provides the possibility for an in-depth analysis of the computed solutions of the TISE and TDSE via full distribution functions [59], variances and quantum fluctuations [54, 55, 59] of observables, and correlation functions [2, 54, 59, 66]; the MCTDH-X software has been benchmarked against exact results [1, 2], verified against experimental predictions [55], and recently reviewed in [4].

The objective, workflow and usage of the MCTDH-X software is introduced in section 2 and exemplified by a detailed tutorial in section 3, where ground states and dynamics of both bosons and fermions are inspected. Our focus is on introducing the usage of the software; details about the MCTDH-X theory are only complementarily discussed where necessary. We conclude and summarize our work in section 4.

2. Structure of the MCTDH-X software

2.1. Objective and main functionality

The objective of the MCTDH-X software is to numerically solve the TISE or TDSE for a given many-body Hamiltonian, which describes N interacting, indistinguishable bosons or fermions subject to a confining potential, and to analyze the computed solutions. A general Hamiltonian has the form

$$\hat{H} = \sum_{i=1}^{N}\left[-\frac{1}{2}\partial_{\mathbf{x}_i}^2 + \hat{V}(\mathbf{x}_i; t)\right] + \sum_{i<j}^{N} \hat{W}(\mathbf{x}_i, \mathbf{x}_j; t), \tag{1}$$

that can be either explicitly dependent on time or not. Here, $\mathbf{x}_i$ is the coordinate of the ith particle, $-\frac{1}{2}\partial_{\mathbf{x}}^2$ is the kinetic energy operator, $\hat{V}(\mathbf{x}; t)$ is a general, possibly time-dependent, one-body potential, and $\hat{W}(\mathbf{x}, \mathbf{x}'; t)$ is a general, possibly time-dependent interparticle interaction operator. The symbol $\hat{}$ denotes operators. All the quantities are given in dimensionless units. The length scale L can be chosen to appropriately represent the physical problem; the corresponding time and energy scales are then determined as $mL^2/\hbar$ and $\hbar^2/(mL^2)$, respectively. In particular, in the presence of a harmonic confinement potential, it is natural to choose the time scale as the inverse of the harmonic trapping frequency ω, i.e. $L = \sqrt{\hbar/(m\omega)}$.

The time-independent many-particle Schrödinger equation (TISE) corresponding to the Hamiltonian of equation (1) is

$$\hat{H}|\Psi_E\rangle = E|\Psi_E\rangle, \tag{2}$$

while the time-dependent Schrödinger equation (TDSE) is

$$\hat{H}|\Psi(t)\rangle = i\partial_t|\Psi(t)\rangle. \tag{3}$$

Note that $\hat{H}$ in the TISE needs to be a time-independent Hamiltonian. In equation (2), $|\Psi_E\rangle$ is an eigenstate of $\hat{H}$ with eigenvalue (energy) E. $|\Psi(t)\rangle$ stands for the solution of the TDSE at time t. Technically, the MCTDH-X software is currently capable of accurately computing few lowest-in-energy eigenstates using Davidson or short iterative Lanczos routine from the Heidelberg MCTDH package [67].

The MCTDH-X theory [26, 27] uses an ansatz for the wavefunction that is a time-dependent superposition of time-dependent many-body basis states:

$$|\Psi(t)\rangle = \sum_{\vec{n}} C_{\vec{n}}(t)|\vec{n}; t\rangle; \quad \vec{n} = (n_1, \ldots, n_M)^T;$$
$$|\vec{n}; t\rangle = \mathcal{N}\prod_{i=1}^{M}[\hat{b}_i^{\dagger}(t)]^{n_i}|\text{vac}\rangle; \qquad \phi_j(\mathbf{x}; t) = \langle\mathbf{x}|\hat{b}_j(t)|0\rangle. \tag{4}$$

Here, the $C_{\vec{n}}(t)$ are referred to as coefficients, the $|\vec{n}; t\rangle$ as configurations, and the normalization factor is $\mathcal{N} = \frac{1}{\sqrt{\prod_{i=1}^{M} n_i!}}$ for bosons and $\mathcal{N} = \frac{1}{\sqrt{N!}}$ for fermions. Each configuration is a fully symmetric or fully anti-symmetric many-body basis state built from M orthonormal time-dependent single-particle states, or *orbitals*, $\{\phi_k(\mathbf{x}, t); k = 1, \ldots, M\}$. The orbitals form an incomplete basis of the Hilbert space which is optimized to represent the many-body wavefunction with a minimal error. The orbitals may be transformed to the eigenfunctions of the reduced one-body density matrix, i.e., the so-called natural orbitals (see below in section 2.2), via a unitary transformation. To fully specify the solution of the TISE or TDSE, the MCTDH-X software computes and stores the coefficients $C_{\vec{n}}(t)$ and the orbitals $\{\phi_k(\mathbf{x}, t); k = 1, \ldots, M\}$ at times t that are specified by the user.

The set of equations of motion for the parameters in equation (4) comprises a coupled set of first-order differential equations for time-dependent coefficients $C_{\vec{n}}(t)$ and nonlinear integro-differential equations for the orbitals $\phi_j(\mathbf{x}; t)$. The details about these equations of motion and their derivation can be found, for instance, in [3, 4, 26, 27]. The MCTDH-X software solves these equations of motion using the so-called constant mean-field integration scheme (see, for instance, [21, 26]). The constant mean-field scheme features an adaptive time step for which the equations of motion for the coefficients and the orbitals are decoupled.

We note that the equation for the orbitals contains the inverse of the matrix elements of the one-body density matrix. In cases where the reduced one-body density matrix has zero eigenvalues and is not invertible, the orbital equations are therefore undefined and problematic. In almost all practical cases and, particularly, for the computations we present below, the regularization strategy documented in [21]—*a posteriori* adding negligibly small eigenvalues to make the inversion possible—is sufficient. More elaborate schemes to improve or avoid this regularization have been developed [68, 69].

2.2. Quantities of interest

Once the coefficients $C_{\vec{n}}(t)$ and the orbitals $\phi_k(\mathbf{x}, t)$ are computed, the MCTDH-X software can analyze the solution $|\Psi(t)\rangle$ and calculate several quantities of interest. These include, respectively, the real-space and momentum-space density distributions

$$\rho(\mathbf{x}) = \langle\Psi|\hat{\Psi}^{\dagger}(\mathbf{x})\hat{\Psi}(\mathbf{x})|\Psi\rangle/N, \tag{5}$$

$$\tilde{\rho}(\mathbf{k}) = \langle\Psi|\hat{\Psi}^{\dagger}(\mathbf{k})\hat{\Psi}(\mathbf{k})|\Psi\rangle/N, \tag{6}$$

the Glauber one-body and two-body correlation functions

$$g^{(1)}(\mathbf{x}, \mathbf{x}') = \frac{\langle\Psi|\hat{\Psi}^{\dagger}(\mathbf{x})\hat{\Psi}(\mathbf{x}')|\Psi\rangle}{N\sqrt{\rho(\mathbf{x})\rho(\mathbf{x}')}}, \tag{7}$$

$$g^{(2)}(\mathbf{x}, \mathbf{x}') = \frac{\langle\Psi|\hat{\Psi}^{\dagger}(\mathbf{x})\hat{\Psi}^{\dagger}(\mathbf{x}')\hat{\Psi}(\mathbf{x}')\hat{\Psi}(\mathbf{x})|\Psi\rangle}{N^2\rho(\mathbf{x})\rho(\mathbf{x}')}, \tag{8}$$

and the natural orbitals $\phi_i^{(\mathrm{NO})}$ and the orbital occupations ρ_i, which, respectively, are the eigenfunctions and eigenvalues of the reduced one-body density matrix

$$\rho^{(1)}(\mathbf{x}, \mathbf{x}') = \frac{1}{N}\langle\Psi|\hat{\Psi}^{\dagger}(\mathbf{x}')\hat{\Psi}(\mathbf{x})|\Psi\rangle = \sum_i \rho_i\phi_i^{(\mathrm{NO}),*}(\mathbf{x}')\phi_i^{(\mathrm{NO})}(\mathbf{x}). \tag{9}$$

Here $\hat{\Psi}^{\dagger}(\mathbf{x})(\hat{\Psi}(\mathbf{x}))$ is a field operator that creates (annihilates) a particle at position $\mathbf{x}$. The natural orbitals are ranked in the order that the first orbital has the highest occupation while the last orbital has the lowest $\rho_1 \geqslant ... \geqslant \rho_M$. Another important quantity, the correlation order parameter (COP), is defined as the sum of the squares of the orbital occupations ρ_i [58, 59]

$$\Delta = \sum_{i=1}^M \rho_i^2. \tag{10}$$

The Glauber correlation functions and the orbital occupations are related to each other. When only the first orbital is macroscopically occupied and thus $\Delta \approx 1$, the system is in a coherent state. In this case, both the one-body and two-body correlation functions for large N are unity, $g^{(1)}(\mathbf{x}, \mathbf{x}) = g^{(2)}(\mathbf{x}, \mathbf{x}) = 1$. The many-body wavefunction Ψ of the system is a product of the same single-particle wavefunction ψ, $\Psi(\mathbf{x}_1,...,\mathbf{x}_N) = \prod_{i=1}^N \psi(\mathbf{x}_i)$. When more than one orbital is macroscopically occupied and thus $\Delta < 1$, the system is *fragmented*. In this case, the Glauber correlation functions become non-trivial and differ from unity. For the sake of brevity, above and in the following we omit the dependence of quantities on time unless when imperative or instructive.

Even more importantly, the MCTDH-X software can simulate single-shot images [55–59]. These single-shot images are the standard way to measure quantum many-body systems of ultracold atoms [70–73]. We note here that single-shot images were also recently simulated, chiefly for mixtures of different species of ultracold atoms, with ML-MCTDH-X, see [74] and references by Mistakidis *et al.* therein. By simulating such single-shot images, the MCTDH-X software can reproduce the quantum measurements in the laboratory. In real space, a single-shot image can be obtained by drawing random positions $(\tilde{\mathbf{x}}_1, \tilde{\mathbf{x}}_2\ ...\ \tilde{\mathbf{x}}_N)$ distributed according to the probability

$$P(\mathbf{x}_1, ..., \mathbf{x}_N) = |\Psi(\mathbf{x}_1, \mathbf{x}_2,...,\mathbf{x}_N)|^2. \tag{11}$$

A similar definition holds in momentum-space too. Due to the presence of quantum fluctuations and correlations, a single-shot image, which is distributed according to $|\Psi|^2$, can be drastically different than the density distributions $\rho(\mathbf{x})$, $\tilde{\rho}(\mathbf{k})$ in equations (5) and (6). The deviation of single-shot images from the density distributions is especially significant when the particle number is small and/or the quantum correlations are large.

A large collection of single-shot images can be used to provide information on the system and particularly on its correlations and phases. Below, we consider a total number of N_{shot} images, with the value of the ith image at position x given by $\mathcal{B}_i(\mathbf{x})$, and provide two types of single-shot analyses:

1. *Single shots for particle correlations* between the two wells of a double-well potential: for each shot, the number of particles in one well, $n_i = \sum_{\mathbf{x}}' \mathcal{B}_i(\mathbf{x})$, is calculated. Here, Σ' indicates that the summation is within a certain well (left or right). We then calculate the probability of finding $n = n_i$ particles in the considered well among all single-shot images

$$P(n) = \frac{N_n(n_i = n)}{N_{\mathrm{shot}}}, \quad n \in \{0, 1, 2, ..., N\}, \tag{12}$$

   where $N_n(n_i = n)$ denotes the total number of shots with $n_i = n$. We will show that the distribution of this probability depends on the correlations between particles.

2. *Quantum fluctuations* can also be extracted from single-shot images [55–59]. To quantify the position-dependent quantum fluctuations of the particle number, we calculate the variance $\mathcal{V}(x)$ from single-shot simulations as:

$$\mathcal{V}(\mathbf{x}) = \frac{1}{N_{\text{shot}}} \sum_{i=1}^{N_{\text{shot}}} \mathcal{B}_i^2(\mathbf{x}) - \left[\frac{1}{N_{\text{shot}}} \sum_{i=1}^{N_{\text{shot}}} \mathcal{B}_i(\mathbf{x}) \right]^2. \tag{13}$$

All these quantities above are chosen because of their accessibility in experiments and direct comparability to experimental results. For example, the momentum-space density distribution is accessible by time-of-flight measurements, the one-body particle correlations are accessible from thermodynamic quantities like kinetic energy [75], and single-shot images are the standard way of measuring cold-atom systems [70–73]. Other quantities of interest currently available in the MCTDH-X software include, for instance, the Glauber one-body and two-body correlation functions in momentum space [76] and many-body entropies of the system [77]. We note that the MCTDH-X software provides the full many-body wavefunction and therefore, in principle, any desired and computationally feasible quantity of interest can be computed with it.

2.3. Workflow

The MCTDH-X software mainly consists of two programs:

1. The main program, `MCTDHX`, computes the numerical solution $|\Psi\rangle$ of the TISE or TDSE.

2. The analysis program, `MCTDHX_analysis`, analyzes the found solution $|\Psi\rangle$.

Here and in the following, we use the `verbatim` font to refer to code, including executable commands, files, statements, and variables.

To set up a numerical task, the user modifies and chooses the parameters via the text input file `MCTDHX.inp`. A detailed description of the available options is given in the manual [78] of the MCTDH-X software. The file `Get_1bodyPotential.F` is used to specify custom one-body potentials [$\hat{V}(\mathbf{x}_i; t)$ in equation (1)], while the file `Get_Interparticle.F` allows for custom two-body potentials [$\hat{W}(\mathbf{x}_i, \mathbf{x}_j; t)$ in equation (1)]. For custom (initial) states, the `Get_Initial_Coefficients.F` and `Get_Initial_Orbitals.F` files can be used to specify the (initial) coefficients $C_{\vec{n}}(t = t_0)$ [see $C_{\vec{n}}(t)$ in equation (4)] and orbitals $\{\phi_k(\mathbf{x}; t = t_0),\ k = 1, \ldots, M\}$ [see $\phi_j(\mathbf{x}; t)$ in equation (4)], respectively.

The workflow and structure of the MCTDH-X software follows naturally from its main objectives to determine a numerical solution to the TISE or the TDSE and then to extract desired quantities of interest from the solution. This workflow can be summarized in the following steps, which are also visualized in figure 1:

---

1. *Determine the initial state.*

    (a) Default: compute the ground state of some Hamiltonian $\hat{H}$ by running `MCTDHX` and configuring the numerical task ('relaxation mode', Hamiltonian, integration procedure etc) in the input file `MCTDHX.inp`.

    (b) Advanced: manually set the coefficients and orbitals that determine the initial wavefunction via the files `Get_Initial_Coefficients.F` and `Get_Initial_Orbitals.F`

2. *Analyze the initial state* by choosing the desired quantities of interest in `analysis.inp` and running the analysis program `MCTDHX_analysis`

    (a) Default: call supplied visualization scripts or `gnuplot` to obtain plots or videos of the results

    (b) Advanced: create custom visualizations or customize supplied visualization scripts

3. *Compute the time-evolution of the initial state* with given Hamiltonian $\hat{H}$. The dynamics of the system is obtained by choosing the numerical task ('propagation mode', Hamiltonian, integration procedure etc.) in the input file `MCTDHX.inp` and running `MCTDHX`.

4. *Analyze the computed time-evolving state* by choosing the desired quantities of interest in `analysis.inp` and running the analysis program `MCTDHX_analysis`. Visualization of the results as in step 2.(a) and 2.(b).

The scripts in the MCTDH-X software generally fall into two categories: either scripts to automate computations like parameter scans or scripts to visualize data in plots and videos. A series of tutorial videos illustrating the workflow step-by-step is available at https://tinyurl.com/tjx35sq. Convergence tests on different variables, including orbital number and grid size, are needed to ensure the accuracy of the simulations. A discussion on the convergence, particularly in orbital number, can be found in the supplementary material
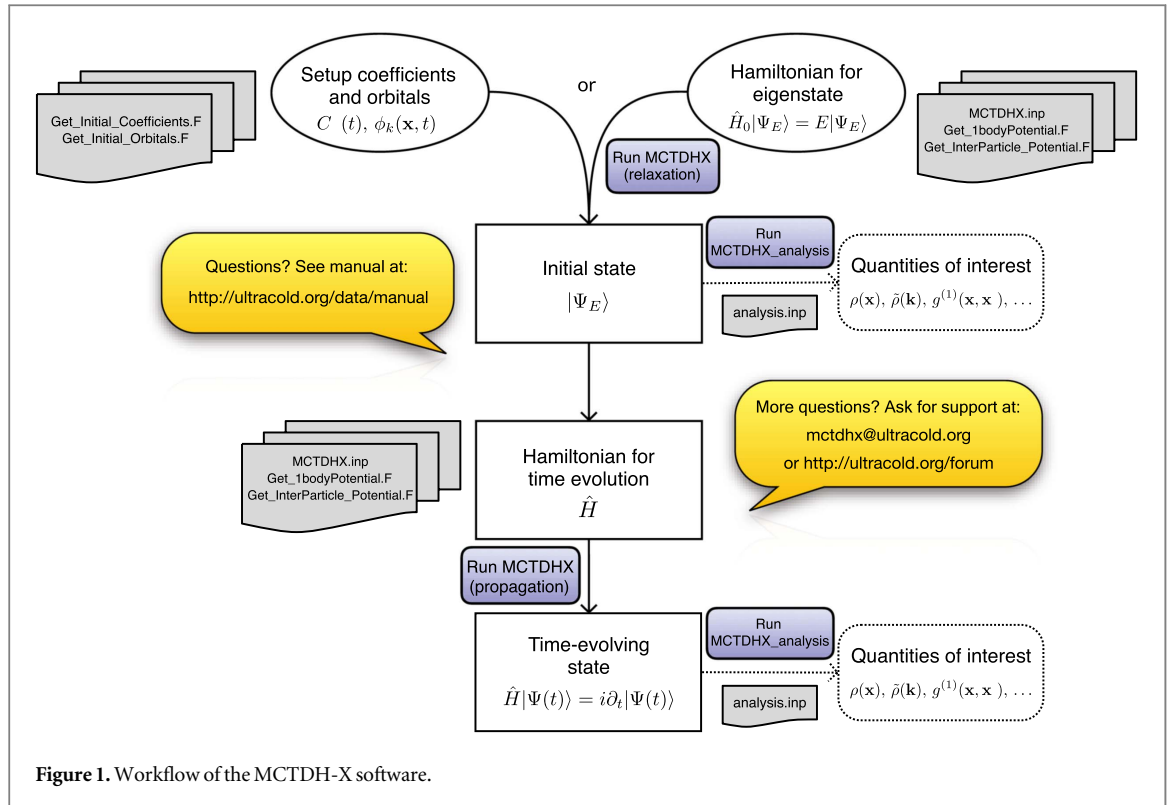
Figure 1. Workflow of the MCTDH-X software.

available online at stacks.iop.org/QST/5/024004/mmedia[9] (including [79–84]). For support and documentation, the website of the MCTDH-X software, http://ultracold.org [37], the MCTDH-X manual [78], and the email address mctdhx@ultracold.org are available. Feature requests should be directed towards the support email address and/or be discussed on the web forum.

3. Tutorial and application

As a tutorial example, we use the MCTDH-X software to study bosons and fermions in one-dimensional double-well one-body potentials $\hat{V}$. The double-well potential has a simple Hamiltonian, and is experimentally relevant [85–87]. Importantly, seen as a lattice with two sites, the double-well potential can be used as a demonstration on how we can use the MCTDH-X software to reveal the static and dynamical properties of the building blocks of lattice systems, i.e. periodic structures of potential wells. Such periodic structures are particularly interesting since they are commonly seen in nature and also synthesized in laboratories. Cold atom systems serve as a convenient platform for the observation of quantum phase transitions [88], since ultracold gases offer an astonishing flexibility—for instance, the lattice depth and the inter-particle interaction strength can be varied almost at will. Choosing a minimal example like the double well reduces the computational difficulty and improves the clarity of our presentation. Nevetheless, some phenomena emerging in large lattices cannot be captured correctly with a simple two-site picture, for instance the Peierls transition, or the realization of the SSH model [89, 90].

The TISE and TDSE for lattices are a cornerstone in many other complex physical systems studied in condensed matter physics, ultracold atoms and quantum gases, quantum computers, materials, and more. Typically, the Hamiltonian for lattices (the above-discussed periodic potential) is approximated by the so-called Hubbard Hamiltonian (see stacks.iop.org/QST/5/024004/mmedia and footnote 9 for details). This approximation uses a basis of static, potentially suboptimal site-localized functions, which are called Wannier functions. The Hubbard model for bosons features the the celebrated 'superfluid to Mott insulator' transition as a result of the competition between the hopping between neighboring lattice sites and the on-site interaction [88, 91]. The double-well potential, though having only two lattice sites, also displays well this transition when varying the barrier between the two wells [92].

A superfluid state of bosons is formed in a shallow lattice, where all particles in neighboring sites 'communicate' and flow freely. It is characterized by quantum coherence between particles in distinct sites of the

---

[9] Supplementary information (SI) includes details about redoing the computations in the main text, and a discussion of the convergence of MCTDH-X computations and of the correspondence of our results with the Hubbard models. The SI further includes [79–84].

lattice. Such coherence results from the fact that all bosons occupy the same single-particle state, i.e. $|\Psi\rangle \sim |N, 0, ...; \, t\rangle$. In contrast, for deep lattice potentials, the particles are localized inside each site, forming a 'frozen' or insulating state analogous to the Mott insulator known from condensed matter physics. In a Mott-insulating state, all bosons in one potential well occupy the same single-particle state. Consider, for example, the wavefunction $|\Psi\rangle \sim |N/2, N/2, 0, ...; \, t\rangle$ for N (here even) bosons in a double well. As a result, the Mott insulator state is characterized by the incoherence of particles between lattice sites.

The coherence and incoherence between sites in a lattice are also reflected in MCTDH-X simulations. In MCTDH-X, to correctly simulate a Mott insulator state, each lattice site requires its own orbital. If the number of orbitals M is smaller than the number of lattice sites, two lattice sites have to 'share' the same orbital, the emergence of Mott-type correlations between these two sites thus cannot be captured correctly. With a sufficient number of orbitals, the coherence and incoherence between sites are accessible through quantities like the correlation functions [equations (7)] or the reduced density matrix and its eigenvalues, which are straightforwardly available in simulations with the MCTDH-X software.

Even though the Bose–Hubbard model is a successful model, it is quite simplistic and cannot capture all the rich physics that might emerge from the solutions of the Schrödinger equation. MCTDH-X is able to capture the physics *beyond* the Bose–Hubbard physics, by virtue of its general basis set which is time-dependent, variationally-optimized, and not necessarily localized at sites. These include a multi-band Bose–Hubbard model (see stacks.iop.org/QST/5/024004/mmedia and footnote 9) and the fermionization of bosons. Specifically, situations where a Hubbard description breaks down have been found, and the improved accuracy offered by MCTDH-X is discussed in [50, 52, 93].

In our examples, we follow and illustrate the workflow described in section 2. We first investigate the ground states and, subsequently the time evolution of one-dimensional setups with bosonic and fermionic particles, which are subject to double-well potential and repulsive interactions. The notation $\mathbf{x}$ will be replaced by x in the following. We also drop the symbol $\hat{}$ for simplicity.

The double-well potential is modeled as a combination of an external harmonic confinement and a central Gaussian barrier. In *natural* units, the MCTDH-X length $L = \sqrt{\hbar/m\omega}$ and energy $E = \hbar\omega$ scales are chosen according to the harmonic trapping frequency ω. In these natural units, the double-well potential we consider is

$$V_{\mathrm{dw}}(x_i) = \frac{1}{2}x_i^2 + E_{\mathrm{dw}}\exp(-2x_i^2). \tag{14}$$

The two minima to the left and to the right of the Gaussian barrier correspond to two lattice sites, as visualized by the orange lines in figures 2(a), (d), (g), (j), (m). The hopping strength of an analogous Hubbard model is mainly controlled by the barrier height, E_{dw}, while the on-site interaction is mainly determined by interaction strength, g (see supplementary material (see stacks.iop.org/QST/5/024004/mmedia and footnote 9) for details on the Hubbard model).

The interaction between the particles is chosen as contact interaction for bosons,

$$W_B(x_i, x_j) = g\delta(x_i - x_j), \tag{15a}$$

and regularized Coulomb interaction for fermions,

$$W_F(x_i, x_j) = \frac{g}{\sqrt{|x_i - x_j|^2 + \alpha^2 \exp(-\beta|x_i - x_j|)}}, \tag{15b}$$

where $g > 0$ is the repulsive interaction strength, $\delta(x)$ is the Dirac delta distribution and the parameters $\alpha = 0.1$ and $\beta = 100$ are used as in [3, 94]. These operators substitute W in equation (1) for the respective cases.

For illustration purposes and for the ease of computations, the number of particles is chosen to be small and thus far from the thermodynamic limit in our examples. The finite size of our systems renders the concept of phases and phase transitions less well-defined, because of the lack of non-analyticity in the ground state energy density during transition. In the following, for the sake of simplicity and readability, we will use the terms 'phase' and 'phase transition' for discussing the properties of the quantum states being aware that they are only the finite-size precursors of the true quantum phases in the thermodynamic limit. We will thus categorize states into different phases if they exhibit distinct behaviors of the various quantities of interest discussed in section 2.2.

All input files and scripts of this section are hosted at http://ultracold.org/data/tutorial_input_files.zip and a detailed description on how to do the computations is given in the supplementary material (see stacks.iop.org/QST/5/024004/mmedia and footnote 9) and a series of tutorial videos at https://tinyurl.com/tjx35sq.

3.1. Ground state properties

We first solve the relevant TISE to find the ground state of $N = 6$ bosons or fermions in the double-well potential of equation (14) by propagating the MCTDH-X coefficients $C_{\vec{n}}(t)$ and basis states $\phi_i(x; t)$ in imaginary time [see equation (4)]. We vary the barrier heights E_{dw} and interaction strengths g to investigate where the superfluid-Mott insulator transition happens. This is done by adapting the input `MCTDHX.inp` and running
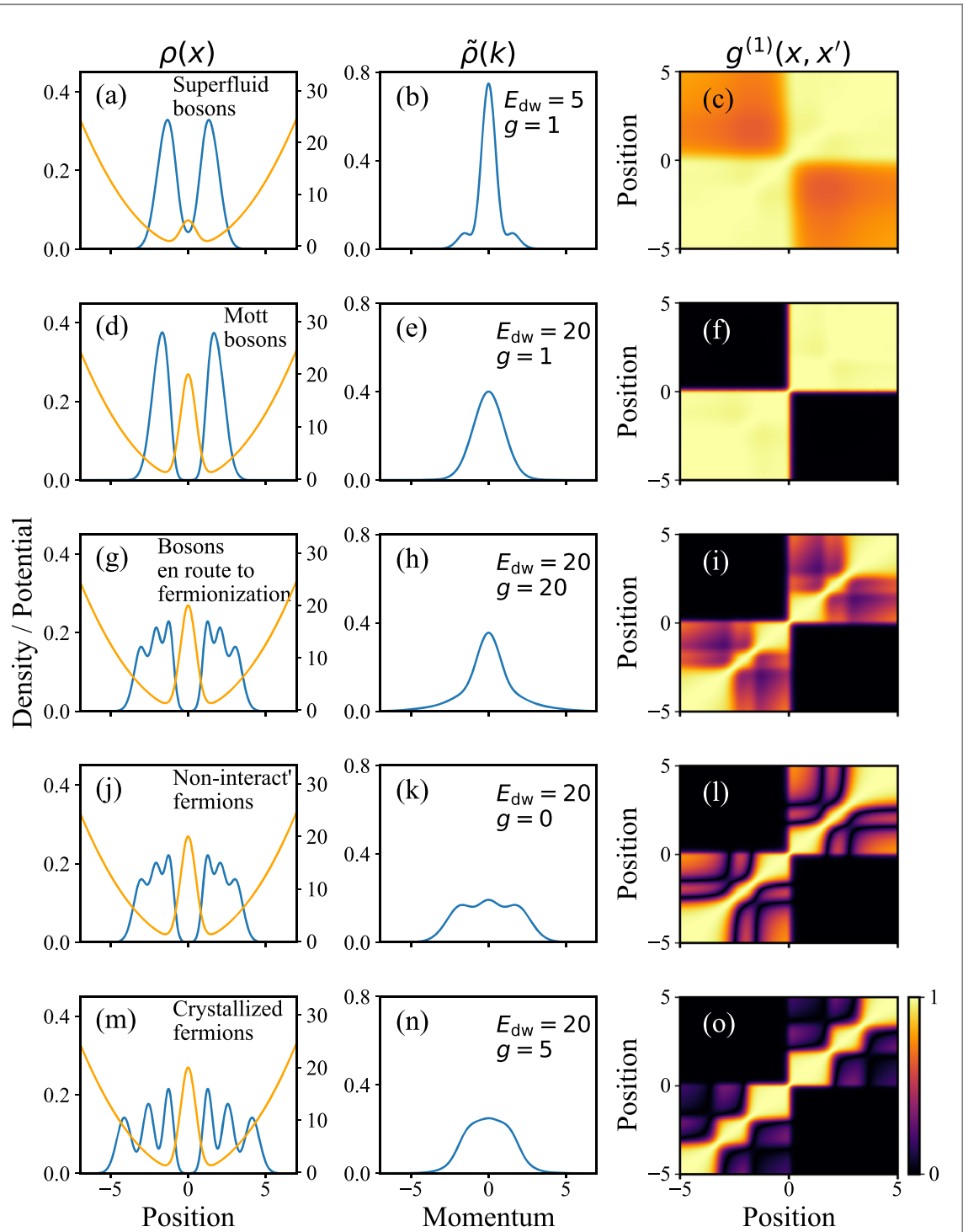
Figure 2. The real-space density distribution $\rho(x)$ (first column, blue lines, label on the left), potential $V(x)$ (first column, orange lines, label on the right), momentum-space density distribution $\tilde{\rho}(k)$ (second column) and the one-body correlation function $g^{(1)}(x, x')$ (third column) of a superfluid bosonic state, (a)–(c), with $E_{dw} = 5, g = 1$ ($\rho_1 \approx 0.831, \rho_2 \approx 0.157$), a Mott insulating bosonic state, (d)–(f), with $E_{dw} = 20, g = 1$ ($\rho_1 \approx 0.497, \rho_2 \approx 0.493$), a bosonic state en route to fermionization, (g)–(i), with $E_{dw} = 20, g = 20$ ($\rho_1 \approx \rho_2 \approx 0.246, \rho_3 \approx \rho_4 \approx 0.152, \rho_5 \approx \rho_6 \approx 0.102$), a non-interacting fermionic state, (j)–(l), with $E_{dw} = 20, g = 0$ ($\rho_1 = \ldots = \rho_6 = 0.167$), and a strongly-interacting crystallized fermionic state, (m)–(o), with $E_{dw} = 20, g = 5$ ($\rho_1 \approx \rho_2 \approx \rho_3 \approx \rho_4 \approx 0.167, \rho_5 \approx \rho_6 \approx 0.165$). There are $N = 6$ particles in all systems. The input files of the simulations are given as simulations #1 to #5 in table S1 of the supplementary material (see stacks.iop.org/QST/5/024004/mmedia and footnote 9).

the program MCTDHX. The number of orbitals is chosen to be $M = 10$. The density distributions in position space and momentum space and the one-body correlation function of the ground states in different potentials are shown in figure 2.

A bosonic superfluid state and a bosonic Mott-insulator state are shown in figures 2(a)–(f), respectively. Compared to the Mott-insulator state, the superfluid state has two extra peaks in momentum space and a non-zero one-body correlation between the two wells $g^{(1)}(x, -x) > 0$. The comparison between these two kinds of

states has been investigated thoroughly with the MCTDH-X software [57, 62, 63, 95] and the results are consistent with other theoretical and experimental results [88, 96, 97]. In this tutorial, we use the terms 'Mott insulating' or 'Mott insulation' to refer to situations where the one-body correlation function [equation (7)] has vanishing values in off-diagonal blocks, i.e. situations where $|g^{(1)}(x, x')| \approx 0$ is true for positions where x and x' are in distinct wells or at the position of distinct peaks of the one-body density, see figure 2(f), for instance.

As the interaction between the bosons further increases, it induces a self-organized lattice-like structure of the density and correlations even within each of the double-well sites [figures 2(g)–(i) for $g = 20$]. This emergence of structure heralds the onset of so-called fermionization; the real-space densities of bosons with large contact interactions approach those of non-interacting fermions [98]. The reason for the emergence of fermionization is that two bosons with infinitely large repulsive contact interactions, like fermions, cannot pass through each other in a one-dimensional system [98]. Such similarities lay the foundation of useful tools like bosonization [99, 100].

However, fermionization and fermionic nature are driven by different mechanisms. This can be intuitively understood through their many-body wavefunctions. The wavefunction of a fermionized state of bosons, $|\Psi_B\rangle$, is still symmetric, while the wavefunction of a non-interacting fermionic state, $|\Psi_F\rangle$, is given by an anti-symmetric Slater determinant built from the first N single-particle eigenstates. In position-space representation $|\Psi_B|^2 \equiv |\Psi_F|^2$ holds true in the fermionization limit; the wavefunctions of bosons and fermions, however, are completely different $\Psi_B(x_1, x_2, \ldots, x_N) = \prod_{i<j} \text{sgn}(x_i - x_j)\Psi_F(x_1, x_2, \ldots, x_N)$ [98]. This difference is reflected in distinct features of the momentum distributions of bosons in the fermionization limit and non-interacting fermions [see figure 2(b), (e), (h), (k), (n) and discussion below].
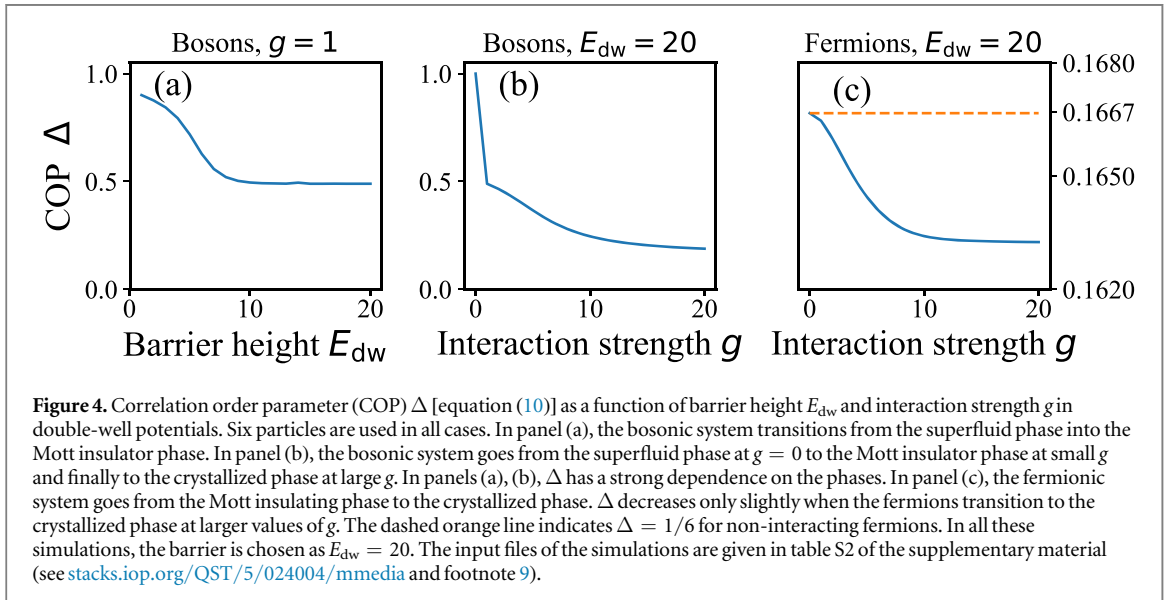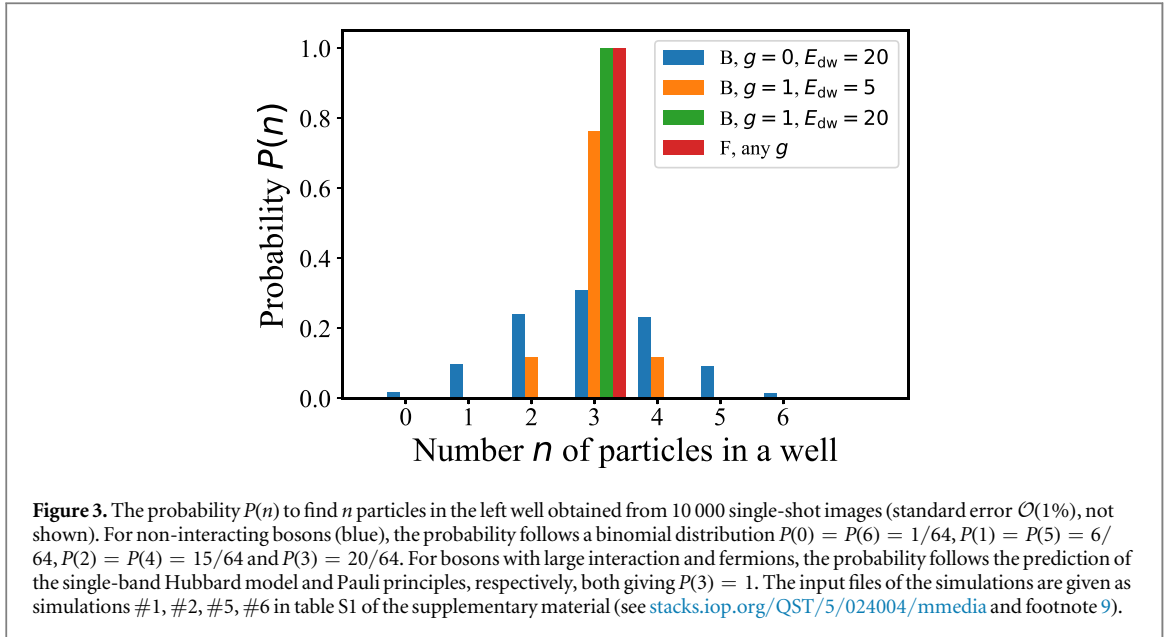
The density distribution at $g = 20$ in figure 2(g) is similar to the one of non-interacting fermions in figure 2(j). The one-body correlation function of the fermions has a complicated pattern of significant and non-trivial correlations [figure 2(l)]. The bosons have a slightly different correlation function than the fermions, but the distinct fermionic pattern is already visible. We thus refer to such states as 'en route to fermionization'. As discussed in [95, 101] and the supplementary material, if an extremely large repulsive interaction and an adequate number of orbitals are used, the fermionization limit can be accurately captured by the MCTDH-X approach [see stacks.iop.org/QST/5/024004/mmedia and footnote 9].

The difference between the bosons en route to fermionization and the fermions, however, appears most explicitly in momentum space. The momentum distribution for the bosons en route to fermionization [figure 2(h)] has the same single-peak structure as the normal Mott insulating bosons [figure 2(e)], where both widths and heights of the peaks are similar. This confirms the similarity between fermionized bosons and Bose–Einstein condensates in momentum space [98]. In contrast, the fermionic state has three peaks in its momentum distribution due to the Pauli principle [figure 2(k)]. These peaks correspond to the three fermions in each well since the two wells are Mott insulating [figure 2(l)].

For long-range dipolar interactions crystallization emerges; for this case, bosons and fermions have been compared, for instance, in [102]. A crystallized bosonic state and a crystallized fermionic state have similar real-space density distributions and they both have many contributing eigenvalues in the reduced one-body density matrix. This indicates that the long-range interaction dominates over the particle statistics. We note that crystallized bosons and fermionized bosons can be distinguished via the spread of their density matrices as a function of the interparticle interaction strength [101].

A fermionic state crystallizes in the presence of sufficiently strong long-range interactions $g = 5$ [see equation 15(b)]. As expected, the repulsive interaction increases the distance between the fermions in real space, see figure 2(m). The interactions also have a pronounced impact in the momentum space distribution [figure 2(n)] and the particle correlations, see figure 2(o). The peaks in the real-space density distribution within each of the wells, which are induced by the Pauli exclusion principle in the absence of interaction [see figures 2(j), (l)], become Mott insulating for crystallized fermions [see figures 2(m), (o)].

The correlations and fluctuations of particles can also be revealed by (simulations of) single-shot images [55–59]. For an illustration of what can be extracted from simulated single-shots, we fix the barrier height $E_{\text{dw}} = 20$ and compute bosonic and fermionic ground states for various interactions g. For every computed state, we generate 10 000 simulated single-shots (adapting `analysis.inp` and running `MCTDHX_analysis`). For each set of single-shot images, we calculate the frequency of $n = 0, \ldots, 6$ particles being in the left well, $P(n)$, and show it in figure 3. For the fermions, each well contains exactly half of the particles regardless of the presence of interactions. This can be seen as a consequence of the Pauli principle. For the bosons, in the superfluid limit $g = 0$, the system is in a coherent state [$g^{(1)} \sim 1$ for all x, x' in figure 2(c)]. In such a coherent state, the distributions of all bosons are independent of each other. As a result of this and the symmetry of the potential, $P(n)$ should be given by the binomial distribution $B(N, 1/2) = \binom{N}{n}/2^N$ and this is confirmed by the single-shot results. As superfluidity gives way to Mott insulation, the distributions of different bosons become interdependent. Due to the repulsive interaction, the Hubbard model predicts that the particles

Figure 3. The probability $P(n)$ to find n particles in the left well obtained from 10 000 single-shot images (standard error $\mathcal{O}(1\%)$, not shown). For non-interacting bosons (blue), the probability follows a binomial distribution $P(0) = P(6) = 1/64$, $P(1) = P(5) = 6/64$, $P(2) = P(4) = 15/64$ and $P(3) = 20/64$. For bosons with large interaction and fermions, the probability follows the prediction of the single-band Hubbard model and Pauli principles, respectively, both giving $P(3) = 1$. The input files of the simulations are given as simulations #1, #2, #5, #6 in table S1 of the supplementary material (see stacks.iop.org/QST/5/024004/mmedia and footnote 9).

Figure 4. Correlation order parameter (COP) Δ [equation (10)] as a function of barrier height E_{dw} and interaction strength g in double-well potentials. Six particles are used in all cases. In panel (a), the bosonic system transitions from the superfluid phase into the Mott insulator phase. In panel (b), the bosonic system goes from the superfluid phase at $g = 0$ to the Mott insulator phase at small g and finally to the crystallized phase at large g. In panels (a), (b), Δ has a strong dependence on the phases. In panel (c), the fermionic system goes from the Mott insulating phase to the crystallized phase. Δ decreases only slightly when the fermions transition to the crystallized phase at larger values of g. The dashed orange line indicates $\Delta = 1/6$ for non-interacting fermions. In all these simulations, the barrier is chosen as $E_{dw} = 20$. The input files of the simulations are given in table S2 of the supplementary material (see stacks.iop.org/QST/5/024004/mmedia and footnote 9).
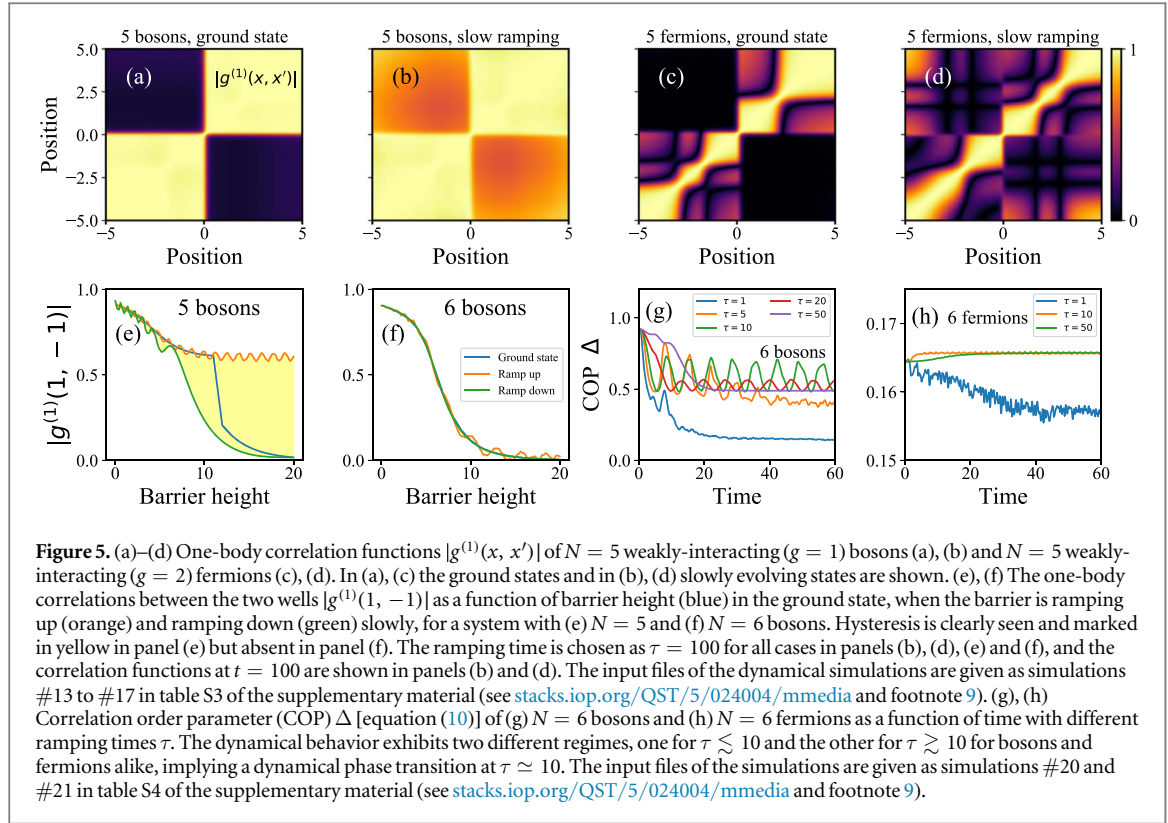
tend to be distributed evenly in each well and $P(3)$ gradually increases while $P(n \neq 3)$ gradually decreases. For our MCTDH-X results in the Mott-insulator limit, $g = 1$, $E_{dw} = 20$, the repulsion between particles becomes so strong that there are exactly three particles in each well $P(3) = 1$ as predicted by the Hubbard model.

The behavior of the system in the superfluid, Mott-insulating crystallized and phases can be summarized and represented by the COP Δ [equation (10)] [58, 59]. The dependence of the COP on the barrier height E_{dw} and interaction strength g in bosonic and fermionic systems is shown in figure 4. In the bosonic system, the COP decreases from almost unity in the superfluid phase to 0.5 in the Mott insulating phase, as expected for a fragmented state with $\rho_1 \approx \rho_2 \approx 0.5$ [figures 4(a) and (b)]. As the interaction strength increases and the system is en route to fermionization, the COP drops further to $\Delta \approx 0.2$. In the fermionic system, Δ is much less sensitive to the interaction strength. It only drops very slightly when the fermions crystallize [figure 4(c)]. The value $\Delta \approx 0.167$ indicates each fermion occupies a single orbital, agreeing with the Pauli principle.

3.2. Dynamical behavior
MCTDH-X is capable of solving the TDSE to capture the dynamics of a system as a reaction to a time-dependent Hamiltonian or to a quench of a parameter. As an example, we prepare the system in the ground state of a harmonic trap, $V_{har}(x) = \frac{1}{2}x^2$ and subsequently, we ramp up a barrier at $x = 0$. We thus smoothly transform

Figure 5. (a)–(d) One-body correlation functions $|g^{(1)}(x, x')|$ of $N = 5$ weakly-interacting ($g = 1$) bosons (a), (b) and $N = 5$ weakly-interacting ($g = 2$) fermions (c), (d). In (a), (c) the ground states and in (b), (d) slowly evolving states are shown. (e), (f) The one-body correlations between the two wells $|g^{(1)}(1, -1)|$ as a function of barrier height (blue) in the ground state, when the barrier is ramping up (orange) and ramping down (green) slowly, for a system with (e) $N = 5$ and (f) $N = 6$ bosons. Hysteresis is clearly seen and marked in yellow in panel (e) but absent in panel (f). The ramping time is chosen as $\tau = 100$ for all cases in panels (b), (d), (e) and (f), and the correlation functions at $t = 100$ are shown in panels (b) and (d). The input files of the dynamical simulations are given as simulations #13 to #17 in table S3 of the supplementary material (see stacks.iop.org/QST/5/024004/mmedia and footnote 9). (g), (h) Correlation order parameter (COP) Δ [equation (10)] of (g) $N = 6$ bosons and (h) $N = 6$ fermions as a function of time with different ramping times τ. The dynamical behavior exhibits two different regimes, one for $\tau \lesssim 10$ and the other for $\tau \gtrsim 10$ for bosons and fermions alike, implying a dynamical phase transition at $\tau \simeq 10$. The input files of the simulations are given as simulations #20 and #21 in table S4 of the supplementary material (see stacks.iop.org/QST/5/024004/mmedia and footnote 9).

the harmonic trap into the double-well potential given in equation (14). We use a linear ramp with a time scale τ

$$E_{\mathrm{dw}}(t) = \begin{cases} E_{\max} t/\tau, & t \leqslant \tau \\ E_{\max}, & t > \tau. \end{cases} \tag{16}$$
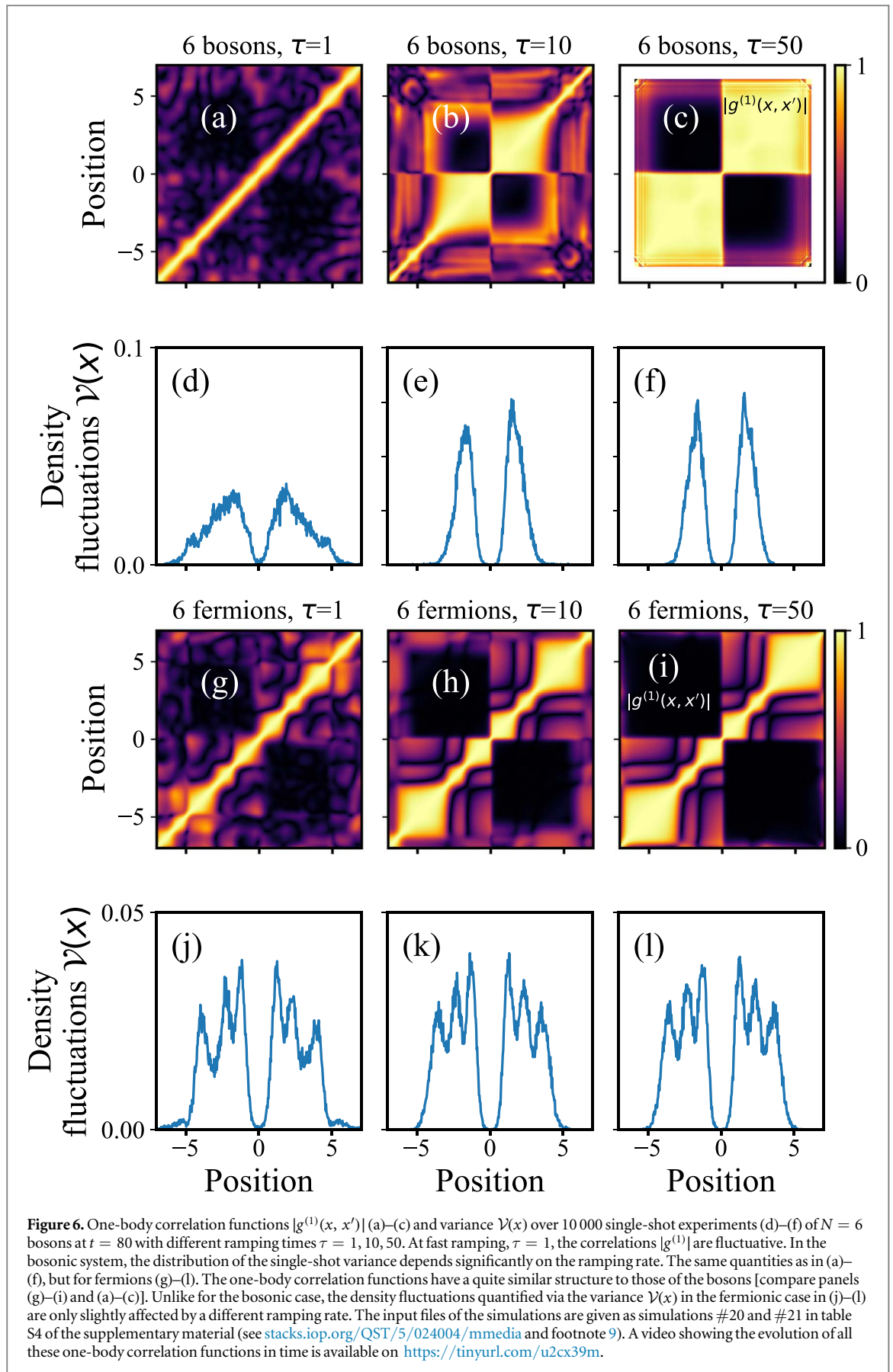
In the following, we compare the states that result for different τ. There are two situations where the resulting state can be different from the ground state of the instantaneous Hamiltonian. (i) If the system undergoes a first-order phase transition—while the parameters of the Hamiltonian change smoothly, the system can get stuck in an excited state of the final Hamiltonian in the absence of a strong perturbation. (ii) With a fast and non-adiabatic change of parameters in the Hamiltonian, excitations are inevitably triggered. Such a quench thus may result in a finite occupation of a large number of eigenstates of the final Hamiltonian [103]. To investigate these two scenarios, we now discuss two examples where the system contains $N = 5$ or $N = 6$ weakly-interacting bosons or fermions.

A first-order transition between a superfluid and a Mott insulator has already been observed in the presence of a three-body interaction [104] in a bosonic system. Such a first-order transition is also observed in our simulations even without three-body interactions, when the total number of bosons or fermions is odd ($N = 5$ in our simulations). There is a large residual correlation $|g^{(1)}(x, -x)| \approx 0.6$ in the time-evolving state—even in the slow evolution limit with ramping time $\tau = 100$ [figures 5(b), (d)] for both the bosonic and the fermionic cases, compared to the ground state where the one-body correlations between the two wells vanish completely [x, x' where $|g^{(1)}| \approx 0$ in figures 5(a), (c)].

The interaction between particles is an essential ingredient in this first-order transition. It lifts the degeneracy between the Mott-insulating state and the state with large residual correlations. However, as the barrier of the double well increases, one of the particles has no preference for entering either of the two wells and thus straddles across both wells. This straddling particle builds up the correlations between the two wells that we observe.

To justify the claim of a first-order transition, we investigate the hysteretical behavior of one-body correlations $|g^{(1)}(1, -1)|$ for $N = 5$ bosons, as shown in figure 5(e). In the ground state, there is clearly a jump at roughly $E_{\mathrm{dw}} \approx 11$. To study the dynamical effects, we choose a ground state in the superfluid limit, $E_{\mathrm{dw}} = 0$ and a ground state in the Mott-insulator limit, $E_{\mathrm{dw}} = 20$. We propagate them in 'opposite directions' across the phase boundary by slowly ramping up (down) the barrier from $E_{\mathrm{dw}} = 0$ to $E_{\mathrm{dw}} = 20$ ($E_{\mathrm{dw}} = 20$ to $E_{\mathrm{dw}} = 0$) in a time of $\tau = 100$. It is clear that there is a hysteresis in the particle correlations. Strikingly, the hysteresis covers an infinite area [see the yellow marked region in figure 5(e)], as the residual correlations will never vanish in the Mott limit. The jump in the correlation functions in the ground states and the hysteresis in the time-evolving states are not seen with an even number of particles [figure 5(f)]. In this even-number case, there is thus a second-order phase transition.

Since the system follows the ground state in the slow limit (large τ) with an even number of particles, we now investigate the effect of a quench (smaller τ) using $N = 6$ bosons or fermions. We ramp up the barrier from zero

Figure 6. One-body correlation functions $|g^{(1)}(x, x')|$ (a)–(c) and variance $\mathcal{V}(x)$ over 10 000 single-shot experiments (d)–(f) of $N = 6$ bosons at $t = 80$ with different ramping times $\tau = 1, 10, 50$. At fast ramping, $\tau = 1$, the correlations $|g^{(1)}|$ are fluctuative. In the bosonic system, the distribution of the single-shot variance depends significantly on the ramping rate. The same quantities as in (a)–(f), but for fermions (g)–(l). The one-body correlation functions have a quite similar structure to those of the bosons [compare panels (g)–(i) and (a)–(c)]. Unlike for the bosonic case, the density fluctuations quantified via the variance $\mathcal{V}(x)$ in the fermionic case in (j)–(l) are only slightly affected by a different ramping rate. The input files of the simulations are given as simulations #20 and #21 in table S4 of the supplementary material (see stacks.iop.org/QST/5/024004/mmedia and footnote 9). A video showing the evolution of all these one-body correlation functions in time is available on https://tinyurl.com/u2cx39m.

to $E_{\mathrm{dw}} = 20$ in three different ramping times, $\tau = 1$, $\tau = 10$ and $\tau = 50$, to which we refer as a fast, an intermediate, and a slow ramp, respectively, in the following. Their one-body correlation functions at a given time, $t = 80$, are shown in figures 6(a)–(c) for bosons and in figures 6(g)–(i) for fermions.

With a slow ramp ($\tau = 50$), the ground state of the final Hamiltonian is recovered—the correlation between the two wells vanishes [see areas where x is to the left (right) of the barrier and x' to its right (left) and $|g^{(1)}(x, x')| \approx 0$ in figures 6(c), (i)]. As the ramping time becomes shorter $\tau = 10$, fluctuations appear on the correlation function, indicating excitations [see areas where x is to the left (right) of the barrier and x' to its right (left) and $|g^{(1)}(x, x')| > 0$ in figures 6(b), (h)]. These excitations accumulate rapidly as the ramping time shortens and, eventually, with a fast ramping $\tau = 1$, we obtain a strongly fluctuating one-body correlation function [figures 6(a), (g)].

To analyze how the quantum fluctuations in the time-evolving states are affected by the speed of the ramp, we quantify the density fluctuations using the position-dependent variance $\mathcal{V}(x)$ [equation (13)] extracted from 10 000 single-shot simulations for bosons in figures 6(d)–(f) and for fermions in figures 6(j)–(l).

Generally, we find the fluctuations are large where the density is large. For bosons, a slower ramp results in an increase of the magnitude of fluctuations [compare figures 6(d)–(f)]. For fermions, the magnitude of fluctuations is practically unaffected by the pace of the ramp [compare figures 6(j)–(l)]. We infer that the behavior of the magnitude of the fluctuations is analogous to the COP Δ [equation (10)]: for bosons, the COP increases a lot as the ramping rate decreases in long time t [see figure 5(g)], whereas the COP varies only very slightly at different ramping rates for the case of fermions [see figure 5(h)]. This analogous behavior of the quantum fluctuations and the COP has previously been used to extract the phases of dipolar ultracold atoms in lattices [58, 59].

The excitations generated by the quench thus also manifest themselves in the eigenvalues of the reduced one-body density matrix or orbital occupations as represented by the COP and its time-dependence [figures 5(g), (h)]. For bosons, in the case of a slow ramp, only two orbitals are macroscopically occupied as in the ground state, while in the case of a fast ramp, the contribution of the first 10 orbitals are of the same order of magnitude and the system is thus highly correlated. The extra fragmentation comes from the dynamics of the system.

For bosons, in the slow case, the COP decreases as the barrier increases and converges to $\Delta = 0.5$ as in the ground state [see figure 4(a)]. As the ramping becomes faster, the COP starts to oscillate and the amplitude becomes larger and larger. However, the dynamical behavior of the COP becomes qualitatively different as the ramping time becomes shorter than $\tau = 10$. It no longer oscillates in a regular manner but rather decreases rapidly and fluctuates. This implies that many high-energy eigenstates of the final Hamiltonian are populated in the dynamics of the system.

For fermions, the absolute values of the orbital occupations are not drastically influenced by the system dynamics and neither is the COP. However, the dynamical behavior of the COP is completely different in the fast and slow ramping limits—in contrast to the bosonic case, the COP increases slightly for a slow ramp, moving closer to the value for non-interacting fermions $\Delta = 0.167$. This indicates that the effects of the interparticle interactions become weaker since the fermions are now divided into two well-separated groups.

The results for the one-body correlation, the COP, and the single-shot simulations point towards a dynamical phase transition at roughly $\tau_C \sim 10$ for fermions and bosons alike. The system behaves like the ground state for ramps slower than τ_C, but becomes highly excited for ramps faster than τ_C.

4. Conclusion and discussions

In this work, we have described and demonstrated the workflow, usage, and structure of the MCTDH-X software hosted, documented and distributed through http://ultracold.org. In a step-by-step tutorial, we have shown how to examine particle correlations and fluctuations using the MCTDH-X software. We have exhibited applications of MCTDH-X to solutions of the time-independent and time-dependent Schrödinger equation for systems of bosons and fermions in a double-well potential. We have computed the many-body wavefunction and calculated various quantities of interest, including correlations, real- and momentum-space density distributions and single-shot experiments. We highlight that our paper demonstrates the first application of MCTDH-X to obtain single shot images for fermions, to analyze correlations via single shot counting statistics, to investigate the dynamical behavior of the COP, and to directly compare the dynamical behavior of bosons and fermions using single-shot images and the COP.

The double-well potential captures many salient features of the Hubbard model, like the superfluid-Mott insulator transition of bosons. Additionally, we find a crystallized state emerging for fermions that bears some similarities with strongly interacting bosons that are en route to the fermionization limit.

In the ground state, we have already observed a wide range of states of fermions and bosons by tuning the interparticle interactions and the barrier height of the double well. Apart from the transition into the Mott phase, the bosonic system approaches the non-interacting fermionic one as the interparticle interactions increase towards the fermionization limit. Fermionized bosonic states have many similarities to non-interacting fermions in the real-space representation. We have demonstrated that the superfluid, Mott insulating,

fermionized, and crystallized phases of many-body states can be distinguished by their correlation functions and by the COP that is a function of the eigenvalues of the reduced one-body density matrix.

Dynamics may drive a system out of the ground state and induce quantum fluctuations and correlations. We have used MCTDH-X to solve the time-dependent Schrödinger equation for bosons and fermions in a one-body potential that is smoothly transformed from a single into a double well by ramping up a Gaussian barrier at different time scales. We have found a novel and unexpected hysteretic behavior that heralds a first-order phase transition for the case of an odd number of bosons or fermions. When the particle number is even, there is no hysteresis, heralding a second-order phase transition. We thus demonstrate that the order of the superfluid-Mott insulator transition depends on the number of particles in our finite-size double-well system. With an odd number of particles, strong residual correlations between the two wells prevail even in the limit of large barriers for any pace of the ramp of the barrier. This implies that the superfluidity of the system cannot be eliminated by increasing the barrier and the system cannot enter the Mott insulator phase dynamically.

For faster ramps, our tutorial example approaches a quench scenario: when the double well's barrier is quenched up rapidly, a considerable amount of eigenstates of the final Hamiltonian become relevantly occupied and participate in the emergent quantum dynamics. This suggests strong fluctuations, which can be confirmed by an analysis of the variance in single-shot images. The significant differences between the fast and slow ramps that we have observed point to a dynamical phase transition.

Finally, we note that although we only have shown examples with a few particles in this tutorial, the MCTDH-X software is able to provide many-body states of systems with a much larger number of particles [105, 106].

Acknowledgments

ORCID iDs

Rui Lin ● https://orcid.org/0000-0001-9560-7187
Elke Fasshauer ● https://orcid.org/0000-0001-8187-6052
Axel U J Lode ● https://orcid.org/0000-0002-8859-1655

References

[1] Lode A U J, Sakmann K, Alon O E, Cederbaum L S and Streltsov A I 2012 *Phys. Rev. A* **86** 63606
[2] Lode A U J 2013 Tunneling dynamics in open ultracold bosonic systems *Springer Theses* (Berlin: Springer)
[3] Fasshauer E and Lode A U J 2016 *Phys. Rev. A* **93** 33635
[4] Lode A U J, Lévêque C, Madsen L B, Streltsov A I and Alon O E 2020 *Rev. Mod. Phys.* **92** 011001
[5] Girardeau M 1960 *J. Math. Phys.* **1** 516
[6] Lieb E H and Liniger W 1963 *Phys. Rev.* **130** 1605
[7] Lieb E H 1963 *Phys. Rev.* **130** 1616
[8] Mcguire J B 1964 *J. Math. Phys.* **5** 622
[9] Calogero F 1969 *J. Math. Phys.* **10** 2191
[10] Sutherland B 1971 *J. Math. Phys.* **12** 251
[11] Dukelsky J and Schuck P 2001 *Phys. Rev. Lett.* **86** 4207
[12] Yukalov V I and Girardeau M D 2005 *Laser Phys. Lett.* **2** 375
[13] Schollwöck U 2005 *Rev. Mod. Phys.* **77** 259
[14] Schollwöck U 2011 *Ann. Phys.* **326** 96
[15] Francisco A R L 2013 *J. Chem. Inf. Model.* **53** 1689
[16] Gross E P 1961 *Nuovo Cim. Ser. 10* **20** 454
[17] Pitaevskii L P 1961 *Sov. Phys.—JETP* **13** 451 (http://jetp.ac.ru/cgi-bin/e/index/e/13/2/p451?a=list)
[18] Alon O E, Streltsov A I and Cederbaum L S 2007 *Phys. Lett. A* **36** 453
[19] Meyer H-D, Manthe U and Cederbaum L S 1990 *Chem. Phys. Lett.* **165** 73
[20] Manthe U, Meyer H D and Cederbaum L S 1992 *J. Chem. Phys.* **97** 3199
[21] Beck M H, Jäckle A, Worth G A and Meyer H D 2000 *Phys. Rep.* **324** 1
[22] Zanghellini J, Kitzler M, Fabian C, Brabec T and Scrinzi A 2003 *Laser Phys.* **13** 1064
[23] Kato T and Kono H 2004 *Chem. Phys. Lett.* **392** 533
[24] Caillat J, Zanghellini J, Kitzler M, Koch O, Kreuzer W and Scrinzi A 2005 *Phys. Rev. A* **71** 12712
[25] Streltsov A I, Alon O E and Cederbaum L S 2007 *Phys. Rev. Lett.* **99** 030402
[26] Alon O E, Streltsov A I and Cederbaum L S 2008 *Phys. Rev. A* **77** 033613
[27] Alon O E, Streltsov A I and Cederbaum L S 2007 *J. Chem. Phys.* **127** 154103
[28] Miyagi H and Madsen L B 2013 *Phys. Rev. A* **87** 062511

[29] Léveque C and Madsen L B 2017 *New J. Phys.* **19** 43007
[30] Léveque C and Madsen L B 2018 *J. Phys. B* **51** 155302
[31] Wang H 2015 *J. Phys. Chem. A* **119** 7951
[32] Manthe U 2008 *J. Chem. Phys.* **128** 164116
[33] Wang H and Thoss M 2003 *J. Chem. Phys.* **119** 1289
[34] Wang H and Thoss M 2009 *J. Chem. Phys.* **131** 24114
[35] Manthe U and Weike T 2017 *J. Chem. Phys.* **146** 64117
[36] Cao L, Bolsinger V, Mistakidis S I, Koutentakis G M, Krönke S, Schurer J M and Schmelcher P 2017 *J. Chem. Phys.* **147** 044106
[37] Lin R, Molignini P, Papariello L, Tsatsos M C, Lévêque C, Weiner S E, Fasshauer E, Chitra R and Lode A U J 2020 *MCTDH-X: The Multiconfigurational Time-Dependent Hartree Method for Indistinguishable Particles Software* (http://ultracold.org)
[38] Lode A U J 2016 *Phys. Rev. A* **93** 63601
[39] Haxton D J, Lawler K V and McCurdy C W 2012 *Phys. Rev. A* **86** 13406
[40] Liao C T, Li X, Haxton D J, Rescigno T N, Lucchese R R, McCurdy C W and Sandhu A 2017 *Phys. Rev. A* **95** 043427
[41] Omiste J J, Li W and Madsen L B 2017 *Phys. Rev. A* **95** 53422
[42] Omiste J J and Madsen L B 2018 *Phys. Rev. A* **97** 13422
[43] Omiste J J and Madsen L B 2019 *J. Chem. Phys.* **150** 084305
[44] Kwasniok S I, Mistakidis and Schmelcher P 2019 arXiv:1911.12839 [cond-mat.quant-gas]
[45] Koutentakis G M *et al* 2019 *New J. Phys.* **21** 053005
[46] Lushuai C, Simeon I. Mistakidis, Xing D and Peter S 2017 *Chem. Phys.* **482** 303
[47] Spekkens R W and Sipe J E 1999 *Phys. Rev. A* **59** 3868
[48] Mueller E J, Ho T-L, Ueda M and Baym G 2006 *Phys. Rev. A* **74** 033612
[49] Streltsov A I, Alon O E and Cederbaum L S 2007 *Phys. Rev. Lett.* **99** 030402
[50] Sakmann K, Streltsov A I, Alon O E and Cederbaum L S 2009 *Phys. Rev. Lett.* **103** 220601
[51] Sakmann K, Streltsov A I, Alon O E and Cederbaum L S 2010 *Phys. Rev. A* **82** 13620
[52] Sakmann K 2011 Many-body Schrödinger dynamics of Bose–Einstein condensates *Springer Theses* (Berlin: Springer) (https://doi.org/10.1007/978-3-642-22866-7)
[53] Sakmann K, Streltsov A I, Alon O E and Cederbaum L S 2014 *Phys. Rev. A* **89** 23602
[54] Weiner S E, Tsatsos M C, Cederbaum L S and Lode A U J 2017 *Sci. Rep.* **7** 40122
[55] Nguyen J H, Tsatsos M C, Luo D, Lode A U J, Telles G D, Bagnato V S and Hulet R G 2019 *Phys. Rev. X* **9** 011052
[56] Sakmann K and Kasevich M 2016 *Nat. Phys.* **12** 451
[57] Lode A U J and Bruder C 2017 *Phys. Rev. Lett.* **118** 13603
[58] Chatterjee B and Lode A U J 2018 *Phys. Rev. A* **98** 053624
[59] Chatterjee B, Schmiedmayer J, Lévêque C and Lode A U J 2019 arXiv:1904.03966
[60] Lode A U J *et al* 2018 *New J. Phys.* **20** 055006
[61] Molignini P, Papariello L, Lode A U J and Chitra R 2018 *Phys. Rev. A* **98** 053620
[62] Lin R, Molignini P, Lode A U J and Chitra R 2019 arXiv:1910.01143
[63] Lin R, Papariello L, Molignini P, Chitra R and Lode A U J 2019 *Phys. Rev. A* **100** 013611
[64] Fischer U R, Lode A U J and Chatterjee B 2015 *Phys. Rev. A* **91** 63621
[65] Chatterjee B, Tsatsos M C and Lode A U J 2019 *New J. Phys.* **21** 033030
[66] Lode A U J, Streltsov A I, Sakmann K, Alon O E and Cederbaum L S 2012 *Proc. Natl Acad. Sci. USA* **109** 13521
[67] Francisco A R L 2013 *J. Chem. Inf. Model.* **53** 1689
[68] Kloss B, Burghardt I and Lubich C 2017 *J. Chem. Phys.* **146** 174107
[69] Meyer H D and Wang H 2018 *J. Chem. Phys.* **148** 124105
[70] Bakr W S, Gillen J I, Peng A, Fölling S and Greiner M 2009 *Nature* **462** 74
[71] Bücker R, Perrin A, Manz S, Betz T, Koller C, Plisson T, Rottmann J, Schumm T and Schmiedmayer J 2009 *New J. Phys.* **11** 103039
[72] Sherson J F, Weitenberg C, Endres M, Cheneau M, Bloch I and Kuhr S 2010 *Nature* **467** 68
[73] Smith D A, Aigner S, Hofferberth S, Gring M, Andersson M, Wildermuth S, Krüger P, Schneider S, Schumm T and Schmiedmayer J 2011 *Opt. Express* **19** 8471
[74] Mistakidis S I, Grusdt F, Koutentakis G M and Schmelcher P 2019 *New J. Phys.* **21** 103026
[75] Cocchi E, Miller L A, Drewes J H, Chan C F, Pertot D, Brennecke F and Köhl M 2017 *Phys. Rev. X* **7** 031025
[76] Lode A U J and Bruder C 2016 *Phys. Rev. A* **94** 013616
[77] Lode A U J, Chakrabarti B and Kota V K 2015 *Phys. Rev. A* **92** 033622
[78] Lode A U J, Tsatsos M C, Fasshauer E, Lin R, Papariello L, Molignini P, Lévêque C and Weiner S E 2020 MCTDH-X Software Manual (http://ultracold.org/manual/)
[79] Dutta S, Tsatsos M C, Basu S and Lode A U J 2019 *New J. Phys.* **21** 053044
[80] Mistakidis S I, Cao L and Schmelcher P 2014 *J. Phys. B: At. Mol. Opt. Phys.* **47** 225303
[81] Mistakidis S I, Cao L and Schmelcher P 2015 *Phys. Rev. A* **91** 033611
[82] Neuhaus-Steinmetz J, Mistakidis S I and Schmelcher P 2017 *Phys. Rev. A* **95** 053610
[83] Mistakidis S I and Schmelcher P 2017 *Phys. Rev. A* **95** 013625
[84] Teichmann N, Hinrichs D, Holthaus M and Eckardt A 2009 *Phys. Rev. B* **79** 100503
[85] Hofferberth S, Fischer B, Schumm T, Schmiedmayer J and Lesanovsky I 2007 *Phys. Rev. A* **76** 13401
[86] Betz T *et al* 2011 *Phys. Rev. Lett.* **106** 20407
[87] Langen T, Erne S, Geiger R, Rauer B, Schweigler T, Kuhnert M, Rohringer W, Mazets I E, Gasenzer T and Schmiedmayer J 2015 *Science* **348** 207
[88] Greiner M, Mandel O, Rom T, Altmeyer A, Widera A, Hänsch T W and Bloch I 2003 *Physica B* **329-333** 11
[89] Su W P, Schrieffer J R and Heeger A J 1979 *Phys. Rev. Lett.* **42** 1698
[90] Su W P, Schrieffer J R and Heeger A J 1980 *Phys. Rev. B* **22** 2099
[91] Jaksch D, Bruder C, Cirac J I, Gardiner C W and Zoller P 1998 *Phys. Rev. Lett.* **81** 3108
[92] Jääskeläinen M and Meystre P 2005 *Phys. Rev. A* **71** 043603
[93] Sakmann K, Streltsov A I, Alon O E and Cederbaum L S 2011 *New J. Phys.* **13** 43003
[94] Bande A 2013 *J. Chem. Phys.* **138** 214104
[95] Roy R, Gammal A, Tsatsos M C, Chatterjee B, Chakrabarti B and Lode A U J 2018 *Phys. Rev. A* **97** 043625
[96] Wessel S, Alet F, Troyer M and Batrouni G G 2004 *Phys. Rev. A* **70** 53615

[97] Kato T and Kono H 2008 *J. Chem. Phys.* **128** 184102

[98] Girardeau M 1960 *J. Math. Phys.* **1** 516

[99] Sénéchal D 2006 *Theor. Methods Strongly Correl. Electrons, 139* (Springer, New York, NY) arXiv:9908262[cond-mat]

[100] Logan D 2004 *J. Phys. A: Math. Gen.* **37** 5275–6

[101] Bera S, Chakrabarti B, Gammal A, Tsatsos M C, Lekala M L, Chatterjee B, Lévêque C and Lode A U J 2019 *Sci Rep* **9** 17873

[102] Deuretzbacher F, Cremon J C and Reimann S M 2010 *Phys. Rev.* A **81** 063616

[103] Frank Schäfer, Miguel A, Bastarrachea-Magnani Axel U J Lode, Laurent de Forges de Parny and Andreas Buchleitner 2020 arXiv:2002.00973 [quant-ph], Entropy 2020 *in press*

[104] Safavi-Naini A, Von Stecher J, Capogrosso-Sansone B and Rittenhouse S T 2012 *Phys. Rev. Lett.* **109** 135302

[105] Klaiman S and Alon O E 2015 *Phys. Rev.* A **91** 063613

[106] Alon O E 2019 *Symmetry* **11** 1344